Gomes *et al. Energy Mater.* **2025**, *5*, 500091
DOI: 10.20517/energymater.2024.297

Energy Materials

Article

Open Access

All-solid-state lithium batteries with NMC_{955} cathodes: PVDF-free formulation with SBR and capacity recovery insights

Beatriz M. Gomes[1,2], Manuela C. Baptista[1,2], Ander Orue[3], Bhattacharjya Dhrubajyoti[4], Sylwia Terlicka[1,5], Peter Sjövall[4], Nico Zamperlin[3], Carlos Fonseca[1,2], Jasmin Smajic[6], Ville Kekkonen[7], Willar Vonk[8], Artur Tron[9], Andy Schena[6], Anwar Ahniyaz[4], Maria Helena Braga[1,2,*]

[1]Engineering Faculty, University of Porto, Porto 4200-465, Portugal.
[2]LAETA, Institute of Science and Innovation in Mechanical and Industrial Engineering, Porto 4200-465, Portugal.
[3]Center for Cooperative Research on Alternative Energies (CIC energiGUNE), Basque Research and Technology Alliance (BRTA), Vitoria-Gasteiz 01510, Spain.
[4]RISE Research Institutes of Sweden, Stockholm 114 28, Sweden.
[5]Institute of Metallurgy and Materials Science, Polish Academy of Sciences, Krakow 30-059, Poland.
[6]Avesta Battery & Energy Engineering (ABEE), Ninove 9400, Belgium.
[7]Pulsedeon Oy Ltd, Tampere 33420, Finland.
[8]TechConcepts B.V., Stolwijk 2821 LE, Netherlands.
[9]AIT Austrian Institute of Technology GmbH, Center for Low-Emission Transport, Battery Technologies, Vienna 1210, Austria.

[*]**Correspondence to:** Prof. Maria Helena Braga, Faculty of Engineering, University of Porto, R. Dr. Roberto Frias s/n, Porto 4200-465, Portugal. E-mail: mbraga@fe.up.pt

How to cite this article: Gomes, B. M.; Baptista, M. C.; Orue, A.; Dhrubajyoti, B.; Terlicka, S.; Sjövall, P.; Zamperlin, N.; Fonseca, C.; Smajic, J.; Kekkonen, V.; Vonk, W.; Tron, A.; Schena, A.; Ahniyaz, A.; Braga, M. H. All-solid-state lithium batteries with NMC_{955} cathodes: PVDF-free formulation with SBR and capacity recovery insights. *Energy Mater.* **2025**, *5*, xx. https://dx.doi.org/10.20517/energymater.2024.297

Received: 21 Dec 2024 **First Decision:** 14 Jan 2025 **Revised:** 15 Jan 2025 **Accepted:** 21 Jan 2025 **Published:** xx Apr 2025

Academic Editors: Xiongwei Wu, Jinping Liu **Copy Editor:** Ping Zhang **Production Editor:** Ping Zhang

Abstract

The nickel-rich NMC_{955} ($LiNi_{0.90}Mn_{0.05}Co_{0.05}O_2$) cathode, with minimal cobalt, is the zenith of $LiNi_xMn_yCo_{1-x-y}O_2$ (NMC) technology but faces structural and thermal stability challenges, losing an average of 15% of its capacity in the first discharge. Here, by selecting appropriate materials and synthesis methods in an all-solid-state battery cell, this challenge is effectively mitigated. A sustainable fabrication of the $LiNMC_{955}$ positive electrode, excluding poly(vinylidene fluoride) (PVDF) and using styrene-butadiene rubber, demonstrates high retention in all-solid-state cells, without additional interlayers or pressure, at room temperature. To prevent oxygen release, spurious phase formation, and magnetic frustration, simulations determined optimal cycling thresholds and curve morphologies for a $Li^0/Li_6PS_5Cl/NMC_{955}$ cell by "following the electrons". This optimized routine ensures prolonged

cycle life and performance demonstrated by sheet resistance/Hall effect, Scanning Electron Microscopy/Energy-Dispersive X-ray Spectroscopy (SEM/EDX), Atomic Force Microscopy/Scanning Kelvin Probe Microscopy, Time-of-Flight Secondary Ion Mass Spectrometry, Raman, calorimetry, and electrochemical analyses. The tailored preparation method and cycling regimen enabled the fabrication of a high-performance cathode, achieving capacities exceeding 110-120 mAh.g^{-1} at C discharging C-rate, after 200 cycles, with a self-recovering component shifting performance to theoretical capacities (192 mAh.g^{-1}), emphasizing the cathode's pivotal role in all-solid-state performance.

Keywords: Li batteries, all-solid-state, NMC, Li_6PS_5Cl, cathode, wet process

INTRODUCTION

Conventional lithium-ion batteries (LIBs) are approaching their energy density limits due to using traditional active materials and liquid organic electrolytes[1-5]. The active cathode material plays a crucial role as it usually defines the specific capacity of the batteries[6]. Various cathode active materials have been refined recently, including $LiNi_xMn_yCo_{1-x-y}O_2$ (NMC)[7-10], $LiNi_{1-x-y}Mn_xAl_yO_2$ (NMA)[11,12], $LiFePO_4$ (LFP)[13-16], $LiMn_{0.6}Fe_{0.4}PO_4$ (LMFP)[17,18], and $LiNi_yMn_{2-y}O_4$ (LNMO)[19-21]. These materials have the potential to enhance cell performance and stability. Among them, NMC-based batteries have gained popularity in the market[22], becoming the dominant cathode material in electric and hybrid vehicles and other electronic devices[19]. The synergy of nickel, cobalt, and manganese in the NMC structure contributes to high specific energy and structural stability of the cathode and lithium-ion diffusion processes[22,23], leading to enhanced performance and extended cycle life.

Several stoichiometries of NMC have been reported, such as NMC_{333}, NMC_{532}, NMC_{622}, NMC_{721}, NMC_{811}, and $LiNi_{0.90}Mn_{0.05}Co_{0.05}O_2$ (NMC_{955})[9]. The first NMC_{333} commercialized was unable to meet the demand for electric vehicle applications. Consequently, a modification was implemented, increasing the Ni content, which resulted in enhanced capacity, rate performance, and lifetime[22]. Sustainability was also an important factor, as decreasing the amount of cobalt is of utmost urgency[11,24].

However, the adoption of this Ni-rich material must be carefully considered, as structural stability issues may arise when the Co^{3+} ions decrease relative to the $Ni^{3+/4+}$ content, leading to diminished effectiveness of Co^{3+} as a buffer ion to alleviate magnetic frustration due to $Ni^{3+/4+}$ paramagnetic character[9,22]. A rock salt structure may form at the surface of NMC as a degradation product during battery operation, for example, by charging to high voltages (> 4.2 V)[25] or due to aging ($Li_xNiO_{2-\delta}$: oxygen deficiency due to lattice oxygen release; $Ni_{1-\delta}O$: reduced nickel oxide phase due to oxygen loss). The formation of a rock salt structure in NMC is typically undesirable as it can lead to performance degradation, including capacity loss (SoC~75%)[25] and increased impedance. Higher nickel content, as in NMC_{955}, generally enhances energy density but can also increase the likelihood of structural transformations under stress[25].

One way to reduce the structural instability of these Ni-rich cathodes is to choose a tailored fabrication method[9] and rigorous electrochemical cut-offs while cycling, allowing the recovery of the cell as shown in calorimetric results hereafter. The preparation method affects the physical and electrochemical properties of the cathode material. Therefore, selecting cathode preparation methods compatible with the industry is crucial, thus ensuring a cost-effective scaling process. The most popular method for cathode industrial production is the wet method[22,26,27], which allows for precise control of the composition, mixture uniformity, and particle morphology necessary to achieve optimal electrochemical performance[9] impeding the formation of spurious phases at the surface (e.g., spinel and rock salt). This study presents a novel wet

fabrication method for a cathode featuring a nearly cobalt-free active material, NMC_{955} [Figure 1].

To enhance battery safety, a departure from conventional liquid electrolytes led to the adoption of a solid-state sulfide electrolyte, Li_6PS_5Cl (LPSCl)[28,29], distinguished for its good ionic conductivity[30] compared to liquid counterparts. To improve the interface between the cathode and electrolyte, a percentage of solid electrolyte was mixed in the cathode solution [Figure 1]. The herein-reported results do not require the use of any additional interlayer for increased stability as required by previously reported literature[31,32], pressure or temperature above room temperature.

Adding the electrolyte to the cathode solution requires the search for chemically compatible binders and solvents[30]. The poly(vinylidene fluoride) (PVDF) binder is commonly used in LIBs[33]. However, its use is nearing its end as the European Union plans to eliminate potential sources of environmental contamination by fluorinated organics[34]. This decision entails banning the manufacture and use of per- and polyfluoroalkyl substances (PFAS), including PVDF. PFAS has come under intense scrutiny in Europe due to mounting evidence of their toxic effects on human health and the environment[34,35]. This decision increases the need to select alternative binders to develop new generations of batteries[36]. PVDF mixed with a polar solvent such as N-methyl-2-pyrrolidone (NMP) is not compatible with LPSCl as it reacts, making it unsuitable as a binder in the herein proposed all-solid-state battery. A comprehensive literature review and an analysis of its properties[30,36-39], such as low polarity, identified styrene-butadiene rubber (SBR) as a potential binder used with toluene as a solvent. SBR is a binder commonly used on the anode side for graphite silicon-based materials[40] and has also begun to be employed on the cathode side, such as NMC[41,42] and LNMO[43,44]. SBR enhances the flexibility of electrodes and strengthens their adhesion[40]. However, this binder has been primarily implemented in cells containing liquid electrolytes[40-42,45]. Herein we report its application to all-solid-state batteries. Control studies using PVDF and SBR as binders in NMC_{955} cathodes, using liquid electrolytes, show that SBR performs better than PVDF, even in liquid electrolyte cells [Supplementary Figure 1].

To ensure the cell is guarded against detrimental spurious reactions affecting their longevity[46,47], it is paramount to accurately determine the charge and discharge potential cut-offs and capacities to avoid reducing (discharge) or oxidizing (charge) the cathodes to voltages at which a different charge carrier (h^+) becomes predominant and the cathode oxidized. In other words, the number of free electrons, $\bar{e}$, in the cathode solid solution should equalize the number of available cations (Li^+) until the charge cut-off voltage is achieved. For each electron, one Li^+ ion is transported from/to the electrolyte from the cathode as acknowledged. Therefore, understanding the advantages of incorporating a constant voltage (CV) step during both cycling processes (charge and discharge) is essential to achieve a high-performance battery[14,48] with charge/discharge control. Electrochemical analyses, Time-of-Flight Secondary Ion Mass Spectrometry (TOF-SIMS), Raman, and calorimetry will later support this necessity.

A series of simulations [Figures 1 and 2, Supplementary Figure 2] were conducted to address the aforementioned questions regarding the present materials[13,15,28]. The objective was to identify the optimal parameters for the electrochemical cycles of the NMC_{955} active cathode material. It involved determining pinpoint voltages, phases, capacities, cut-offs, and electrical properties such as cathode conductivity and density of states (DOS) (Experimental Section).

EXPERIMENTAL

Materials

The cathode material was meticulously prepared using a mixture of 57% NMC_{955} (Huayou New Energy

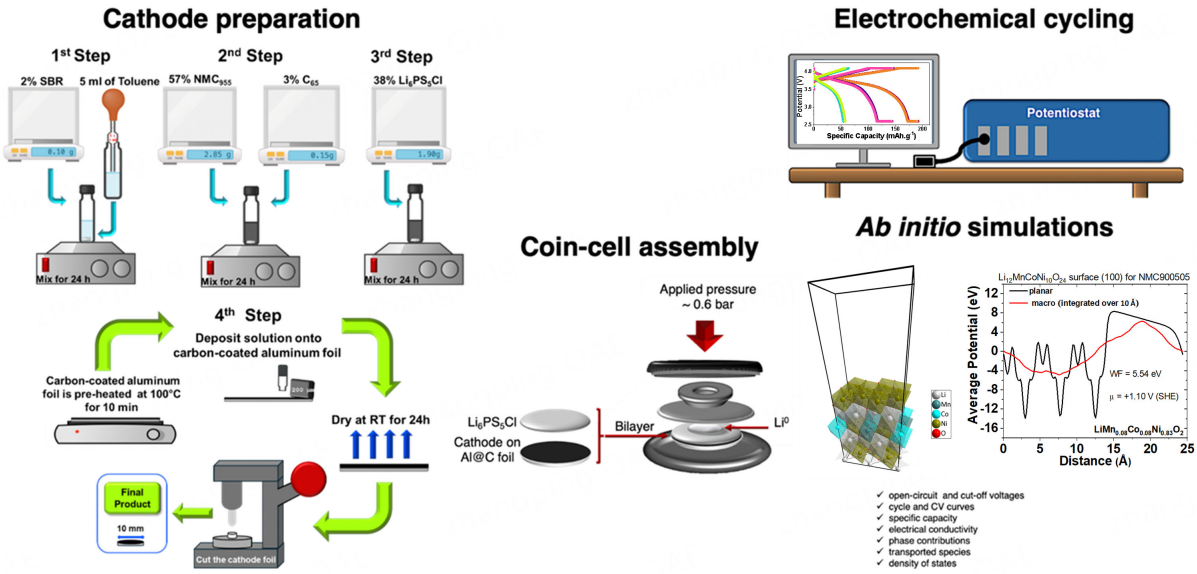

Figure 1. Summary of the adopted methodology. Left: cathode fabrication process using a wet method developed inside a glove box. Center: resulting cathode incorporated into an all-solid-state coin cell, assembled in the glove box. Right: visual representation of the testing procedure and *ab initio* simulations related to battery materials and experiments.

Technology), 38% LPSCl (NEI corporation), 3% Active Carbon (TIMCAL graphite & carbon super C_{65}), and 2% binder (SBR-1502 KUMHO, cold-polymerized SBR, containing 23.5 at/wt. % styrene, HB Chemical). The solvent used in this solution was toluene (Honeywell, purity ≥ 99.7%).

Cathode preparation

The preparation process involved four main steps [Figure 1]: 1st the binder SBR was mixed with 5 mL of toluene for 24 h; 2nd NMC_{955} and C_{65} were added to the solution and mixed for another 24 h; 3rd the electrolyte was introduced to the last mixture, and all was stirred for an additional 24 h, and 4th using a 4-side film applicator with a thickness of 200 μm; the resulting slurry was deposited onto a pre-heated Al foil coated with carbon (at 100 °C for 10 min.) and left to dry for at least 24 h. After drying, the prepared cathode film was cut into discs of a 10 mm diameter using a disk drilling machine for a coin-cell electrode cutter from TMAX-CN. All steps were performed inside the GS Glovebox (O_2 < 1 ppm and H_2O < 1 ppm). A detailed microstructural study of the resulting materials was performed after depositing the cathode material on an Al-coated carbon substrate (MSE Supplies LLC) of 15 μm thickness.

Cell fabrication and electrochemical characterization

A bilayer of the previously prepared cathode material and LPSCl solid electrolyte was formed. To achieve this, 100 mg of LPSCl was pressed onto the cathode disk for one minute at 1 ton, using a mold with a 10 mm diameter and the SPECAC press machine. The CR2032 coin cells were fabricated according to the structure depicted in Figure 1. The anode material used was pure lithium metal, supplied by Goodfellow, with a thickness of 200 μm and 8 mm diameter. The areal capacities of the cathodes vary from 0.167 $mAh.cm^{-2}$ to 2.17 $mAh.cm^{-2}$, calculated based on the active area of the cathode, which is constrained by the size of the anode and considering the theoretical capacity of 192 $mAh.g^{-1}$. The cells were closed using a digital pressure-controlled electric crimper for coin cells MSK-160E. Once the cells were assembled, the electrochemical performance was assessed by a series of electrochemical tests. Three types of measurements were performed. Firstly, potentiostatic electrochemical impedance spectroscopy (PEIS) tests were performed to determine the internal resistance using a Biologic VMP-300 potentiostat. The PEIS

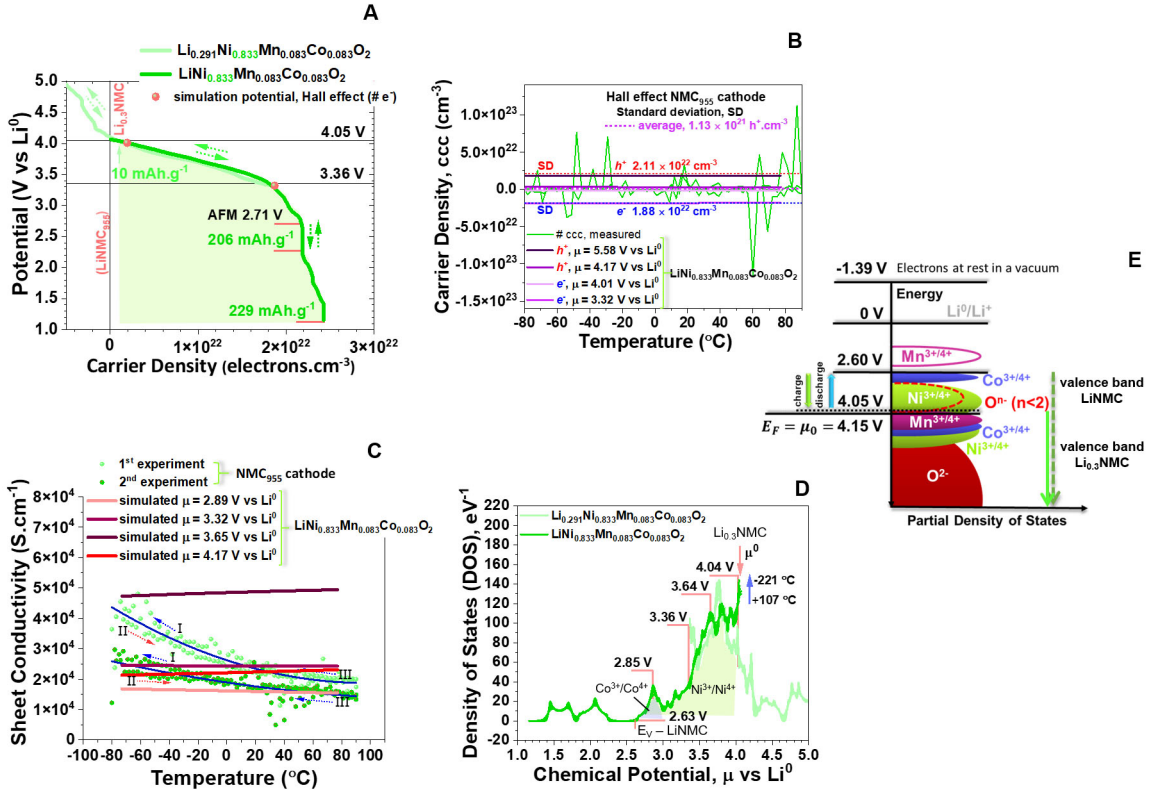

Figure 2. *Ab initio* simulations on ($LiNMC_{955}$) = $Li_{12}Ni_{10}MnCoO_{24}$ = $LiNi_{0.833}Mn_{0.083}Co_{0.083}O_2$ and ($Li_{0.29}NMC_{955}$) = $Li_7Ni_{20}Mn_2Co_2O_{48}$ = $Li_{0.291}Ni_{0.833}Mn_{0.083}Co_{0.083}O_2$ using DFT. (A) Simulated potential *vs.* electron carrier density (+electrons; -holes) for ($LiNMC_{955}$) and ($Li_{0.29}NMC_{955}$); (B) charge carriers concentration *vs.* temperature (-electrons; +holes): experiments by Hall effect with the cathode 57% NMC_{955}+38% Li_6PS_5Cl+3% C_{65}+2% SBR and simulations for different chemical potentials for ($LiNMC_{955}$); (C) sheet conductivity *vs.* temperature for the same cathode and simulations for different chemical potentials for ($LiNMC_{955}$) *vs.* Li^0; I-first cooling, II-first heating; III-second cooling; (D) simulated electronic DOS *vs.* chemical potential at -221 T (C) 107 for ($LiNMC_{955}$) and ($Li_{0.29}NMC_{955}$) featuring predominant redox pairs. The structures were approximated to NMC_{955} as much as computationally reasonable (between NMC_{811} and NMC_{955}); (E) schematics representing energy vs partial DOS for $LiNMC_{955}$ discharged cathode and correspondent predominant redox pairs. Note: the schematic in E is based on the results obtained with DOS simulations and shown in D. DFT: Density functional theory; SBR: styrene-butadiene rubber; DOS: density of states.

experiments were performed with an alternate current (AC) with an amplitude of ±10 mV for an initial differential potential corresponding to the cell's open circuit voltage (OCV) and the frequency range from 7 MHz to 100 mHz. Subsequently, cyclic voltammetry tests were applied to determine the capacity of the obtained cell using a Biologic VMP-300 potentiostat. The experiments superimposed ±0.1 V to the initial differential potential corresponding to the cell's OCV. The rate ranged from 0.1 up to 50 $mV.s^{-1}$. The cyclic voltammetry measurements were repeated five times, with applied limits for each cycle ranging from 2.0 V to 4.5 V. The galvanostatic charge-discharge (GCD) was performed to evaluate the cyclability and behavior of cells at different C-rates and specific energy. The galvanostatic cycling tests were performed in a Neware-CT-4008Tn-5V-20mA battery tester with 2.6 V and 4.1 V cut-off voltages.

Cathode characterization (Hall effect and sheet resistance)

Hall effect measurements were performed using the Linseis HCS 1 Hall effect measurement system with two magnetic circuits (Neodymium) assembled on a moveable sled. Samples were prepared as positive electrode films, ensuring they were suitable for Hall effect measurements. The prepared sample was then mounted on the sample holder of the Linseis HCS system, with electrical connections established between the sample edges and the input terminals of the measurement system. A perpendicular magnetic field *B*, $B = \pm 0.7$ *T*, was

applied to the sample, and the intensity of the magnetic field was adjustable and accurately measured by the system. A constant current (I) [DC: 1nA up to 125 mA (8 decades/compliance 12 V)] was transported through the sample along its length. The Hall voltage (V_H), generated perpendicular to the applied current and the magnetic field, was measured [DC: low noise/low drift 1 μV up to 2,500 mV, 4 decades amplification, digital resolution: 300 pV]. This voltage arises due to the Lorentz force acting on the charge carriers within the sample. Hall voltage measurements were recorded for various magnetic field intensities and current values to ensure accuracy, with multiple measurements conducted for repeatability. The Hall coefficient (R_H) was calculated using $R_H = \frac{V_H d}{IB}$, where d is the sample thickness. The charge carrier density ccc_{Hall}, n, and the mobility μ' were subsequently determined using $n = \frac{1}{eR_H}$ and $\mu' = \frac{R_H \sigma}{e}$, where e is the elementary charge and σ the conductivity of the sample measured as follows.

Samples were prepared with a uniform thickness suitable for sheet resistance measurements. Following the Van der Pauw method, four collinear electrical contacts were attached to the samples when mounted on the sample holder, and electrical connections were made to the measurement system. A constant current (I) was applied between two adjacent contacts on the sample, and the voltage (V) was measured between the remaining two adjacent contacts. Measurements were taken in different configurations, rotating the contacts to ensure precision and consistency, with multiple readings recorded for each configuration. The sheet resistance (R_S) was calculated using $R_S = \frac{V}{I} f$, where f is a geometrical correction factor, typically close to 1, depending on the contact configuration and sample geometry. For the Van der Pauw method, the relationship $e^{-\pi R_{s1}/R_s} + e^{-\pi R_{s2}/R_s} = 1$ is used, where R_{S1} and R_{S2} are resistances measured in perpendicular directions.

All measurements were conducted in a controlled environment. The system was evacuated to 10^{-2} bar, and subsequently, an N_2 flux of 4-5 L/min, was used to minimize spurious reactions, temperature fluctuations, and external noise.

The results were analyzed to determine the Hall coefficient, carrier concentration, mobility, and sheet resistance. They were then compared with theoretical values and reference materials for validation.

Cathode characterization (scanning electron microscope/energy dispersive spectroscopy and atomic force microscope/scanning kelvin probe microscopy)

A scanning electron microscope (SEM) FEI QUANTA 400 FEG ESEM was used. The chemical composition analysis was performed with an EDAX Genesis X4M energy-dispersive X-ray spectrometer. Microstructural observations and chemical composition analyses were conducted using an accelerating voltage of 15 kV, a spot size between 3 and 5, and a working distance of 10 μm. Images were taken at magnifications ranging from 20× to 20,000×. All images were obtained with a backscattered electron (BSE) detector. To further characterize the cathode material, an Atomic Force Microscope (AFM) capable of conducting Scanning Kelvin Probe Microscopy (SKPM) was employed (Oxford Instruments Atomic Force Microscope MFP-3D Origin$^+$ AFM). The analysis was made with a laser-driven tip with a resonant frequency of approximately 75 kHz ASYELEC-01-R2. The tip material comprises silicon with a reflective coating of Ti/Ir and a spring constant (k) of 2.8 $N.m^{-1}$. The topography analysis was conducted using tapping mode, which consists of gently oscillating the probe over the sample surface to acquire high-resolution topographic information. Simultaneously, this analysis of the SKPM acquisition was performed. SKPM is a non-invasive technique derived from atomic force microscopy that allows the electrochemical characterization of materials.

Cathode characterization (TOF-SIMS and Raman)

TOF-SIMS analyses were carried out in a M6 TOF-SIMS instrument (IONTOF GmbH, Münster, Germany) using 30 keV Bi_3^+ primary ions. The sample was mounted on the sample holder (top-mount, without

contact with the cathode surface) inside a glove box and transferred into the TOF-SIMS instrument using an air-tight transfer vessel (IONTOF GmbH). Positive and negative ion data were recorded in the all-purpose spectrometry mode and the delayed extraction fast imaging mode, over analysis areas ranging from 100 × 100 μm² to 250 × 250 μm². Only negative ion data is presented in this study. Before analysis, the top layers of the sample surface were removed by sputtering using 2 keV Cs^+ ions (58 nA, 600 × 600 μm², 37 s).

The cycled cell used in the TOF-SIMS analysis had an areal capacity of 1.90 mAh.cm^{-2} and was subjected to PEIS, cyclic voltammetry, and electrochemical cycling [Supplementary Figure 3]. The electrochemical potential range was set between 2.6 V and 4.1 V. The cell underwent ten cycles, with three cycles at C/50, 3 at C/20, 3 at C/10, and 1 at C/5 before TOF-SIMS post-mortem analyses.

Raman spectra were collected at room temperature with a Raman spectrometer (Renishaw inVia Confocal Raman, Reinshaw, Wotton-under-Edge, UK) equipped with a laser of 532 nm excitation wavelength focused through an inverted microscope (Leica, Wetzlar, Germany), via a 50× objective. A composite NMC_{955} electrode was placed in an air-sensitive sample holder and the sample preparation was performed inside the glovebox (H_2O, O_2 ≤ 1 ppm).

The cell used for post-mortem Raman testing had a cathode loading of 1.6 mAh.cm² and was cycled between 2.6 V and 4.1 V at a C-rate of C/20 for up to ten cycles. A CV step was introduced during charge and discharge.

Cell characterization (Calorimetry)

Heat flow analysis was conducted using a TAM IV microcalorimeter (TA Instruments), which provides high sensitivity measurements. The experiment was performed at a constant temperature of 30 °C. The cell under investigation was cell CC I [Supplementary Table 1] and consisted of lithium metal as the anode, LPSCl as the electrolyte-separator, and an NMC_{955}-based cathode material. The calorimetric analysis was the final test performed on the cell. For the test, a reference cell was also assembled for comparison, consisting solely of a top cap, bottom cap, separator, and a spring all made of stainless steel. When the heat flow started, the cell displayed an OCV of 3.7 V. To further investigate the internal heat flow behavior, external resistors (217 kΩ and 253 kΩ) were connected to the cell through an external circuit. These resistors allowed for an evaluation of heat flow during the discharge of the battery.

Density functional theory and structural, electronic, and potential energy simulations

In the computational analysis, the study employed density functional theory (DFT)[49], facilitated by the Vienna Ab initio Simulation Package (VASP)[49] code. Simulations were focused on a $[Li_{12}MnCo(Ni_5O_{12})_2]_2$ - $LiNi_{0.833(3)}Mn_{0.083(3)}Co_{0.083(3)}O_2$ (P1) supercells originally optimized from a R-3m (hP18) rhombohedral disordered structure with $a = b = 2.874$ Å and $c = 14.165$ Å and $\alpha = \beta = 90$ and $\gamma = 120$. To the latter disordered structure, Li was randomly removed until it became $Li_7Mn_2Co_2Ni_{20}O_{48}$ - $Li_{0.292}Ni_{0.833(3)}Mn_{0.083(3)}Co_{0.083(3)}O_2$. The DFT simulation was based on DFT and the generalized gradient approximation (GGA)-Perdew-Burke-Ernzerhof (PBE)[50] exchange-correlation functional for describing the interactions. Electronic structure calculations were performed with a cut-off energy of 500 eV and a k-spacing of 0.3 Å^{-1} corresponding to a 5 × 2 × 2 mesh and electronic convergence of 10^{-5} eV. Model-determined non-magnetic and spin-polarized magnetic simulations were performed to compare optimized structures and stabilities (energies of formation). Supercells with (100), (010), and (001) surfaces were built with a > 10 Å vacuum layer to disrupt periodicity for both $[Li_{12}MnCo(Ni_5O_{12})_2]_2$ and $Li_7Mn_2Co_2Ni_{20}O_{48}$ structures [Supplementary Figure 2] and determine the total local potential and its 10 Å integration range macroscopic average potential. The work function (WF), or electrochemical potential $\bar{\mu}$,

determines the energy difference between the vacuum surface and the Fermi-level macroscopic average potentials. The electrochemical potential of a species *i* (element, phase, cathode, current collector,) is $\bar{\mu}_i = \mu_i + e\phi_i$, where μ_i is its chemical potential and ϕ_i indicates its surface potential due to electrical contact with another species or to self-induced surface effects. Hence, if $\phi_i = 0 \Rightarrow \bar{\mu}_i = \mu_i$, which was the assumption used herein, except for cell-like electrical contact between species. When two species *i* and *j* come in electrical contact, the electrochemical potentials tend to equalize, $\bar{\mu}_i - \bar{\mu}_j = 0 = \mu_i - \mu_j + e(\phi_i - \phi_j)$ and, if one of the materials is an insulator such as the LPSCl solid electrolyte, an electrical double layer capacitor (EDLC) with potential difference $\Delta V_{ij} = (\phi_i - \phi_j)$ will be spontaneously formed at the interface of the two species, e.g., electrode/electrolyte where the energy is stored. The potential *vs.* Li^0 simulated and plotted in Figure 2 is $\Delta V_{NMCvsLi^0} = \frac{\mu_{Li^0} - \mu_{NMC955}}{e} = (\phi_{Li^0} - \phi_{NMC955}) = -1.39 - \phi_{MNC955}$ with $\phi_{MNC955} < \phi_{Li^0}$[51]. Charging corresponds to a chemical potential increase of the negative electrode, and a decrease of the chemical potential of the positive electrode (increasing bias potential). Discharging is a spontaneous process and corresponds to the opposite variation of the chemical potentials (decreasing bias potential). The zero-energy reference corresponds to the maximum energy and the energy of the electrons at rest in a surface in vacuum[51]. The capacity in Figure 2 is calculated from the number of charge carriers using *capacity* $= \frac{carrier\_density\,(number\_of\_electrons.cm^{-3}) \times \bar{e}(C)}{\rho(g.cm^{-3})} \frac{1}{3.6}$ (mAh.g^{-1}), where $\bar{e} = 1.6 \times 10^{-19}$C is the elementary charge and ρ = 4.71 g.cm^{-3} the volumetric mass of NMC_{955} simulated herein.

Tools from VASP and Electronics within the MedeA 3.7 software were utilized for calculating chemical potentials μ_i, charge carrier densities *n*, sheet conductivities σ, mobilities μ', electronic band structures, and DOS.

RESULTS AND DISCUSSION

Simulations to determine optimal cycling thresholds

To comprehend the behavior of NMC_{955}, *ab initio* simulations using DFT[49] were performed to determine optimal parameters for testing, such as the potential (V) limits for the electrochemical cycles [Figure 2A] and cycle curve morphologies [Figure 2A]. The cut-off charging voltage was determined to be 4.05 V, coinciding with the (Li_xNMC_{955}) with 0.29 < x < 1 solid solution transforming from ($LiNMC_{955}$) to ($Li_{0.29}NMC_{955}$), and the net number of free electrons reduced to a minimum, corresponding to a capacity of ~10 mAh.g^{-1}. Up to 4.05 V, the slightly more stable solid solution composition is $LiNMC_{955}$ as its chemical potential versus Li^0 is higher. Above 3.36 V, NMC_{955} is a solid solution, a homogeneity region of (Li_xNMC_{955}) with 0.29 ≤ x ≤ 1.00[52]. While discharging to the cut-off potential of 2.60 V, the cell initially charged to $Li_{0.29}NMC_{955}$ shows a theoretical simulated capacity of 196 mAh.g^{-1} per comparison with the calculated from $Li_{0.3}NMC_{955} \leftrightarrow 0.7Li^+ + 0.7\bar{e} + (Li_{0.3}NMC_{955})$: ~192 mAh.g^{-1}.

Herein, the importance of discharging at CV of ~2.60 V becomes clear as the number of free electrons should achieve 2.07 × 10^{22} $\bar{e}$.cm^{-3} corresponding to the fully formed ($LiNMC_{955}$). This allows the cell to be subsequently charged to 4.05 V, forming ($Li_{0.29}NMC_{955}$) and keeping structural stability. The latter leads to a long cycle life corresponding to a primary redox activity involving approximately $0.7Li^+ + 0.7\bar{e}$ + ($Li_{0.29}NMC_{955}$) ($LiNMC_{955}$) and the nickel transitioning from higher to lower oxidation states ($Ni^{4+} \rightarrow Ni^{3+}$) down to 3.00 V. While discharging form the first "shoulder" observed in Figure 2A at 3.12 V to 2.60 V, cobalt may also play a role lowering its oxidation state ($Co^{4+} \rightarrow Co^{3+}$), not substantially affecting the integrity of the (NMC_{955}) structure. The only species found on the cathodes' surface after bombarding the sample with a focused beam of high-energy ions with TOF-SIMS are NiO_2^- and CoO_2^- in agreement with the Ni^{3+} and Co^{3+} discharged species between 4.05 V and 2.6 V [Figure 2E].

The number of charge carriers is measured using the Hall effect with two magnetic circuits with a magnetic field (B_{max} = 0.7 T). A current of 6.7 mA.cm^{-2} is applied to the cathode sheet, and the Hall potential V_H and constant R_H are determined, leading to the charge carrier density or concentration (ccc) calculation (Experimental Section). The ccc_{Hall} resulting from applying the Hall effect to a 1.6 × 2.0 cm^2 NMC_{955} cathode with 57% $LiNMC_{955}$+38% LPSCl+3% C_{65}+2% SBR is directly comparable to the simulated $ccc_{simulated}$ of ($LiNMC_{955}$) for different charged states [Figure 2B]. It should be noted that the cathode in the Hall effect and sheet resistance experiments is charged only with electrons, not with Li^+-ions, as the cathode is not inserted into a battery cell. The simulations match the experiments; for the chemical potential μ = 3.32 V and 4.01 V *vs.* Li^0, the concentration of electrons $\bar{e}$ surpasses the number of cations: electron vacancies and holes, represented by (h^+). For μ = 4.17 V and 5.58 V *vs.* Li^0, h^+ surpasses $\bar{e}$, in agreement with the Hall and electrochemical experiments, indicating that the cathode was over-charged with oxygen (O_2) release possibly occurring [Figure 2E]; it is noteworthy to highlight yet again that the cathode is not charged with Li^+ as it is not charged as a cell component but as a single sheet.

The absolute chemical potential of the solid solution ($LiNMC_{955}$) (coinciding with its Fermi level when electrically insulated with null surface potential) is μ_0 = 4.15 V *vs.* Li^0, corresponding to 2.74 × 10^{21} h^+.cm^{-3} [Figure 2A] obtained by simulating the total local potential for a surface of $Li_{12}Ni_{10}MnCoO_{24}$ [Figure 2, right, Supplementary Figure 2]. It agrees with the chemical potential μ_0 = 4.09 V *vs.* Li^0 of the average of charge carriers concentration ccc_{Hall} = 1.13 × 10^{21} h^+.cm^{-3} in Figure 2B.

Note that the analyzed cathode contained 38% LPSCl electrolyte, a semiconductor with an electronic structure band gap energy of 2.5 eV[28], which may have been under-evaluated by DFT-GGA as traditionally occurs with semiconductors; the band gap may ascend to 4.2 eV. The cathode also contained 3% C_{65}+2% SBR, but other materials besides the active cathode did not considerably affect the experimental results for 0 ≤ T(°C) ≤ 80, as shown for the sheet conductivity in Figure 2C. Below 0 °C, the experimental data marks the behavior of a conductor with increased conductivity as the temperature drops; the presence of carbon black in the cathode may have influenced the conductivity. The simulated data, however, shows an increase in conductivity as the temperature decreases for μ = 2.89 V *vs.* Li^0; for all other values, the material behaves as a semiconductor, as expected for $LiNMC_{955}$ [Figure 2D and E]. All experimental reversible results (common to I, II, and III) fall within the values of the simulated data. The electrical conductivity for the entire range of temperatures increases as the chemical potential rises to μ = 3.65 V *vs.* Li^0 and decreases for μ = 4.17 V *vs.* Li^0, which agrees with the general drop in electrical conductivity as the cathode is charged. The simulated mobility of the charged species is shown in Supplementary Figure 2.

The cathode's surface potential $\phi_{cathode}$, measured by AFM with its scanning kelvin probe (SKP) mode, is 2.71 V *vs.* Li^0, which coincides with the expected OCV from the analysis of Figure 2A and D. The 2.63 V marks the higher voltage of a small band gap with null DOS and the lowest voltage of a region with a high DOS, where the electrochemical cycles should be confined. The DOS steadily decreases above 4.04 V, as expected. The cut-offs of 2.63 V and 4.04 V and the inflection voltage at 3.36 V *vs.* Li^0 represent pinpoints in the DOS *vs.* chemical potential plot of ($LiNMC_{955}$) and ($Li_{0.29}NMC_{955}$) [Figure 2D and E]. The lithiation between 4.04 V and 3.00 V predominantly corresponds to the redox reaction ($Ni^{4+} \rightarrow Ni^{3+}$) and between 3.00 V and 2.63 V to ($Co^{4+} \rightarrow Co^{3+}$). Below 2.24 V, the second "shoulder" gain in capacity is due to the ($Mn^{4+} \rightarrow Mn^{3+}$) transformation [Figure 2A]. However, this extra capacity may be paid for with structural instability as the latter pairs are highly paramagnetic, conversely to ($Co^{4+/3+}$), likely causing magnetic frustration. It is worth noting that the post-mortem analyses of cells that were cycled between 2.6 V and 4.1 V show evidence of small oxidation of the sulfates in the electrolyte on the $LiNMC_{955}$ surface. This oxidation is due to sulfur diffusion and cannot be completely avoided. However, keeping the cell within the

cycling range of 2.6 V to 4.1 V prolongs the cell cycle life by reducing to the barely minimum the oxidation and the formation of rock salts, $Li_xNiO_{2-\delta}$ resulting from oxygen deficiency due to lattice oxygen release, and $Ni_{1-\delta}O$ following from reduced nickel oxide phase due to oxygen loss.

Materials characterization with SEM/energy-dispersive X-ray spectroscopy and atomic force microscopy/SKPM

The microstructure of the active material $LiNMC_{955}$ in powder was analyzed by Scanning Electron Microscopy/Energy-Dispersive X-ray Spectroscopy (SEM/EDX) and presented in Figure 3A. The nano-sized particles of NMC show a relatively irregular size and shape and a tendency to form agglomerations. Additionally, the EDX analysis demonstrates that the atomic Ni:Mn:Co ratio is approximately 90:5:5, consistent with the anticipated composition [Supplementary Table 2]. The cathode discs prepared in this study were also analyzed using SEM/EDX [Figure 3B and C]. A uniform cathode deposition is demonstrated in Figure 3B. By increasing the magnification in Figure 3C, the homogeneous distribution of the active material nanoparticles is observed in detail: light grains, point 2 [Supplementary Table 2]. The dark gray particles correspond to the LPSCl electrolyte, point 1 in Figure 3C. The SBR binder is also apparent, denoted by the black spots uniformly dispersed throughout Figure 3B and C, effectively binding the materials together within the sample. Additional proof of the homogeneous consistency of the cathode is given in Supplementary Figures 4 and 5, with the element distribution maps (C, O, Co, Mn, Ni, Cl, P, and S).

To characterize the prepared cathode foil's topography and surface chemical potential, an AFM with the ability to perform SKPM was used. The topography profile of the cathode is shown in Figure 3D, demonstrating that the cathode is uniform despite nanotopographic "peaks". The corresponding electrochemical profile is shown in Figure 3E and F. As expected, there is no relationship between the topography [Figure 3D] and the electrochemical profile [Figure 3F] and Supplementary Figure 6. In the electrochemical profile [Figure 3F], charge accumulation regions with minimal amplitude can be observed between 0.155 V and -0.845 V *vs.* standard hydrogen electrode (SHE) [Figure 3E], corresponding to 3.205 V and 2.205 V *vs.* Li^0. These results demonstrate that this cathode material exhibits quasi conductor-like behavior despite containing a significant proportion of the semiconductor LiPSCl electrolyte and the insulator SBR. In fact, the potential variation of the stripes in Figure 3E and F may indicate semiconductor behavior with a band gap approximately < 1 V [Figure 2A, D and E] for $LiNMC_{955}$ between 2.6 V and 2.2 V. This observation aligns with the results obtained experimentally and simulated for the conductivity and DOS of the cathode [Figure 2C and D]. Another significant observation is that the average potential of this cathode sample is -0.35 V *vs.* SHE, 2.71 V *vs.* Li^0, and -4.09 eV in the physical scale (absolute scale)[51] where the maximum chemical potential is zero for the electrons at rest in a surface in vacuum. The latter value is within the limit of the anode-cathode typical barrier[13,51].

Electrochemical characterization

The obtained cathode foils were used to assemble all-solid-state batteries with LPSCl as the electrolyte separator and lithium metal as an anode. All cells analyzed in this article are summarized in Supplementary Table 1. After assembly, the cells underwent electrical impedance spectroscopy (EIS) and cyclic voltammetry tests [Figure 4A and B]. The equivalent circuit of the EIS was determined, along with the values of its components. R_1 is an ohmic resistor and corresponds to the resistance to the conduction of most agile species at higher frequencies. It represents asymmetric phenomena mostly occurring at the interfaces. Ideally, R_1 should approach zero. On the other hand, R_2 is the diameter of the first semicircle and corresponds to ionic hoping in a capacitor with no charge accumulation at the interfaces. R_2 refers to the bulk impedance of the dielectric (electrolyte) in a capacitor with $C = \varepsilon_0 \varepsilon_r \frac{A}{d}$, where A is the cross-section area, d is the thickness of the electrolyte, and $\varepsilon = \varepsilon_0 \varepsilon_r$ represents the dielectric constant of the electrolyte, where ε_0

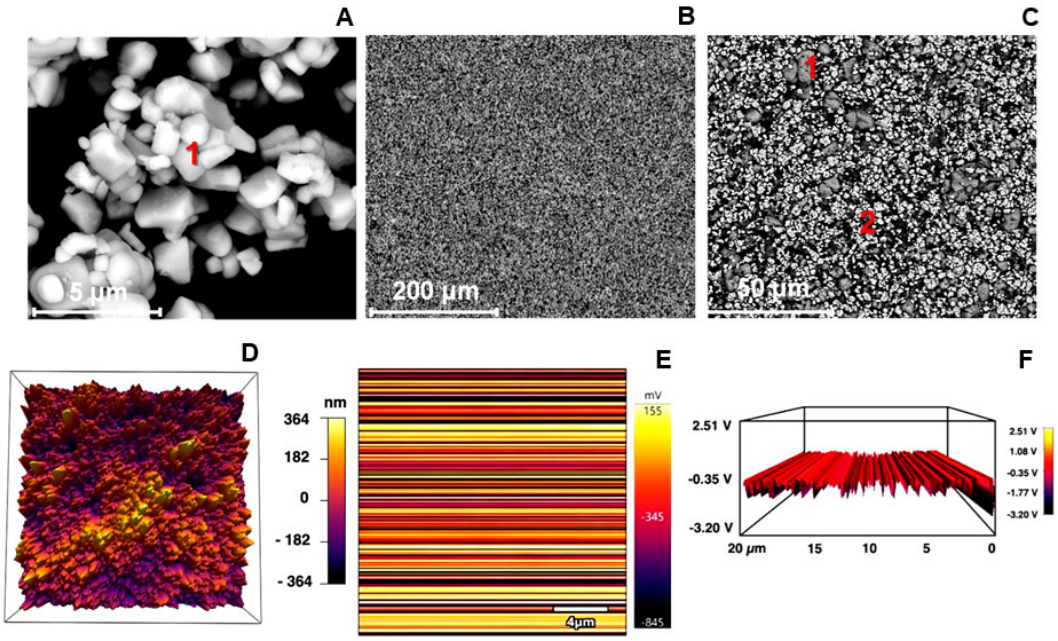

Figure 3. Characterization of cathode materials. SEM/EDX images acquired with the BSE detector of (A) pure NMC_{955} powder at a magnification of 20,000; (B and C) cathode sample of 57% NMC_{955}+38% Li_6PS_5Cl+3% C_{65}+2% SBR at different magnifications 500 and 2,000×. Surface topography of cathode material using atomic force microscopy and SKPM; (D) 3D view; 2D electrochemical profile in (E) and 3D in (F). Note: the electrochemical potentials are plotted as analyzed *vs.* SHE (standard hydrogen electrode); to refer to Li^0: *Vvs* Li^0 = *Vvs SHE* + 3.05. The areal capacity of the cathodes in SEM/EDX (B and C) and atomic force microscopy/SKPM (D-F) analyses is ~0.17-0.20 $mAh.cm^{-2}$. SEM: Scanning electron microscope; EDX: energy-dispersive X-ray spectroscopy; SKPM: scanning Kelvin Probe Microscopy.

is the permittivity of vacuum and ε_r stands for the real relative permittivity of the electrolyte. The resistance of the electrolyte is $R_2 = \frac{1}{\sigma}\frac{d}{A}$ where σ is the ionic conductivity of the electrolyte. The ionic hoping in a solid inorganic electrolyte affects both electrodes simultaneously as Li^+ displacing in a direction implies a Li^+ vacancy charged negatively V_a^- moving in the opposite direction; therefore, the best element to represent the opposition to Li^+ hoping is a resistor in parallel with the correspondent capacitor. The phenomena occurring at the interfaces in Electrical Double Layer Capacitors (EDLCs) are related to Q_3, R_3 and Rd_4 [Figure 4A]. Non-ideal Li^+ diffusion occurs from the EDLCs and the diffusion pathway should only correspond to a small path/thickness in the positive electrode.

The cyclic voltammetry [Figure 4B] clearly show a pronounced reduction peak at 3.3 V while the cell is discharged. Notably, the current's response sharply increases at ≥ 4.0 V, suggesting a shift in charge carrier origin from $\bar{e}$ to h^+ (with possible loss of $O^{\delta-}$), emphasizing the importance of charging at CV, avoiding charging beyond this cut-off voltage. As discussed previously, this limit was also verified in theoretical simulations and experiments in Figure 2. These findings allow the establishment of electrochemical cycling limits ranging from 2.6 V to 4.1 V based on the cyclic voltammetry [Figure 4B], which agree with the simulations in Figure 2.

The cell was subjected to electrochemical cycles at different C-rates according to the estimated electrochemical limits. The theoretical specific capacity of the NMC cathode was considered 192 $mAh.g^{-1}$ since only ~70% of the Li ions were allowed to be delithiated from the cathode material while charging[13]. The best cell performance for each of the implemented C-rates: C/50, C/20, C/10, C/5, C/3, C/2, C, 2C, and 3C are shown in Figure 4C. Based on the electrochemical cycles [Figure 4C], it is marked the significant

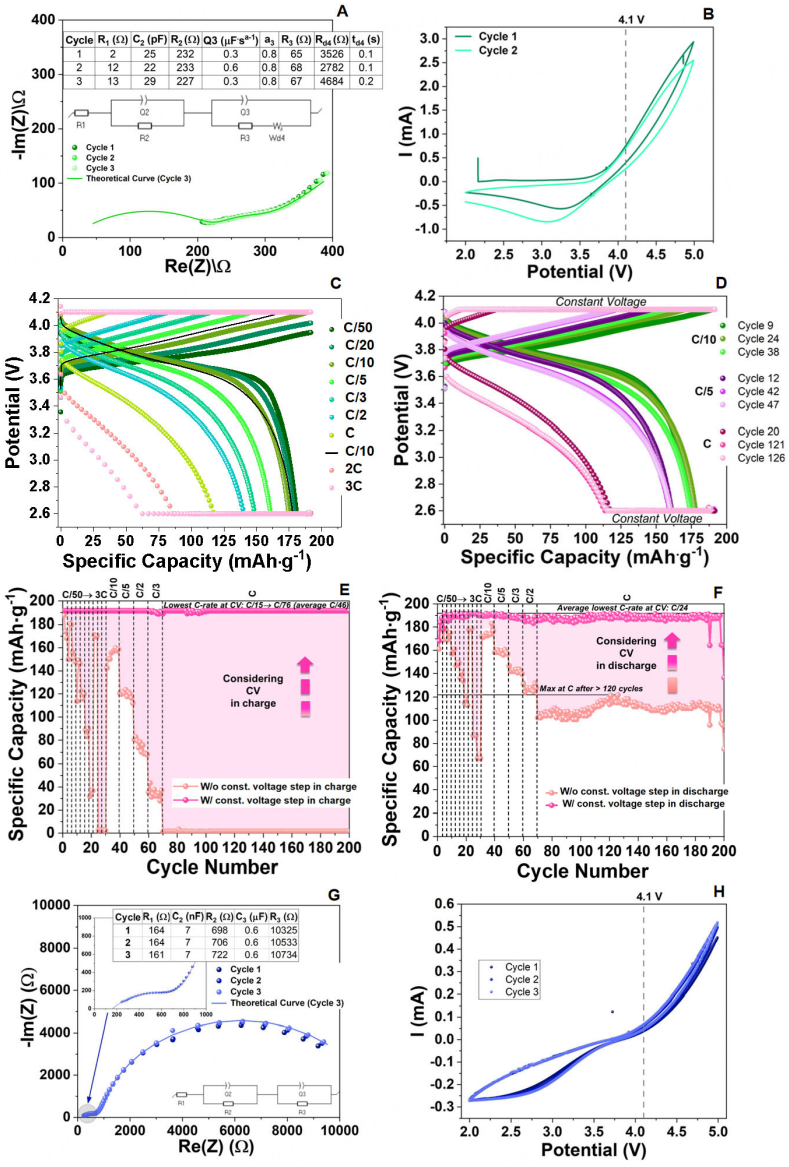

Figure 4. Electrochemical characterization of a cell containing the 57% NMC_{955}+ 38% Li_6PS_5Cl+3% C_{65}+2% SBR cathode with active material $Li^0/Li_6PS_5Cl/NMC_{955}$. (A and B) PEIS and cyclic voltammetry analysis of the cell before the electrochemical cycling; (C) best electrochemical cycles for each C-rate; (D) cycles at C/10, C/5 and C; (E and F) Specific capacity *vs.* cycle number for charge and discharge, respectively, for the following C-rates: C/50, C/20, C/10, C/5, C/3, C/2, C, C/10, 2C, 3C, C/10, C/5, C/3, C/2, and C; (G and H) PEIS and cyclic voltammetry analysis of the cell after the electrochemical cycling. Cells tested at 25 C with no applied pressure; areal capacity of the cathode: 0.167 $mAh.cm^{-2}$. Note: In E the lowest charging C-rate at CV varies from C/15 to C/76 for an average of C/46 and in F the lowest discharging average C-rate at CV is C/24. The maximum discharge capacity at C C-rate is > 120 $mAh.g^{-1}$. SBR: Styrene-butadiene rubber; PEIS: potentiostatic electrochemical impedance spectroscopy; CV: constant voltage.

stability in cell performance.

NMC_{955} cathode materials are prone to safety issues, such as thermal runaway, structural instability, and oxygen release due to the eminent presence of Ni^{2+}[9,22]. Employing appropriate fabrication methods may help mitigate these risks by ensuring uniformity and minimizing the presence of impurities or defects that could trigger unwanted reactions under stressful conditions[22]. From the electrochemical performance in this study, it is evident that this cathode combination enables the creation of stable, long-lasting cells with

unique performance, reaching the theoretical capacity multiple times for different C-rates, Figure 4D and Supplementary Figure 7A and B, showcasing a coulombic efficiency of ~100% considering the CV step in the electrochemical cycling [Supplementary Figure 7C]. Incorporating a CV step during both the charge and discharge stages is crucial for ensuring the cell's long-term performance and little to no Ni^{2+} formed. The redox reactions for nickel are restricted to ($Ni^{4+} \leftrightarrow Ni^{3+}$). This distinction becomes evident while analyzing the maximum discharge capacity obtained in the experiments shown in Figure 4E and F, Figure 5, and Supplementary Figure 7. At the charging process at higher C-rates, the cell's capacity is achieved at CV, as shown in Figure 4E. The discharge at a constant current attains a higher capacity than the corresponding charging step [Figure 4F]. By including a final CV step, the cell repeatedly reaches its theoretical capacity at C for 130 cycles, for a total of 200 cycles. At C above cycle seventy, the lowest charge C-rate range obtained for the CV step was C/15 → C/76, for an average of C/46 [Figure 4E]. In fact, charging at C was found to be impossible above cycle 70, contrary to expectations, as charging is usually conducted faster than discharging in all-solid-state batteries. The average lowest C-rate for the discharge correspondent to the CV step was C/24. At C discharge C-rate, the capacity varied from 100 $mAh.g^{-1}$ to 120 $mAh.g^{-1}$ for a total theoretical capacity of 192 $mAh.g^{-1}$ obtained for almost 200 cycles while accounting for the CV step [Figure 4F].

In Supplementary Figure 7C, the coulombic efficiency versus cycle number with and without the CV step was calculated considering the previous full charge. Otherwise, while cycling at C, where the charge obtained at constant current is almost null and, therefore, the charge is almost fully obtained at CV, the efficiency would always be > 100% for all cycles between 70 and 200 [Supplementary Figure 7A-C]. After completing the electrochemical cycles, PEIS and cyclic voltammetry tests were conducted [Figure 4G and H]. The PEIS profile changed significantly compared to the initial analysis [Figure 4A]. As shown in Figure 4G, the profile now features three semicircles, resembling the PEIS results obtained before the 2C C-rate electrochemical cycles [Supplementary Figure 7D]. An increase in the R_1 value was observed throughout the impedance tests, indicating intensified asymmetric phenomena at the different interfaces. Similarly, the bulk impedance of the electrolyte increased over successive tests. The third semicircle, visible in Figure 4G and Supplementary Figure 7D, lacks a diffusion component that was observed in the initial impedance test [Figure 4A] suggesting a reduced diffusion, contrasting with the initial test where diffusion was evident. Comparing Figure 4G with Supplementary Figure 7D demonstrates a substantial increase in resistance, which may indicate early signs of cell degradation. This is further supported by the cyclic voltammetry curves [Figure 4B and H, and Supplementary Figure 7E], which, while maintaining similar overall behavior, exhibit a measurable decrease in currents at equivalent voltages.

The direct comparison between experiments and stable solid solutions simulations is shown in Figure 5A, where all pinpoints and morphology of the electrochemical curves are observed and compared with the experiments for C/50 and C/10. The simulated capacity is calculated as the difference between the capacity at 2.60 V (lower voltage cut-off) and the capacity obtained when $Li_{0.29}NMC_{955}$ becomes the stable solid solution, at 4.05 V, which happens for a capacity of 10 $mAh.g^{-1}$. Hence, the simulated capacity is 196 $mAh.g^{-1}$ (2%) when compared with the calculated 192 $mAh.g^{-1}$ for a final composition of $Li_{0.3}NMC_{955}$. The resolve to perform CV steps on charge and discharge is evidenced by two Li^0/LPSCl/NMC_{955} cells in Figure 5B and C, Supplementary Figures 8-10. The difference between cells in Figure 5B and C lies in the amount of active material, which directly affects the areal capacity of the cell. Figure 5B shows electrochemical results for cells with areal capacities ranging from 0.2 $mAh.cm^{-2}$ to 0.4 $mAh.cm^{-2}$, while Figure 5C presents data for cells with an areal capacity of approximately 2 $mAh.cm^{-2}$ [Supplementary Figure 10]. In Figure 5B, cell 1 has a similar areal capacity to cell 2; however, when accounting for the CV step for charge and discharge, a capacity gain of > 3× is obtained in cell 1. A capacity gain of > 2× is obtained for cell 2 when comparing the same number of cycles with and without CV step, where the first cycles were

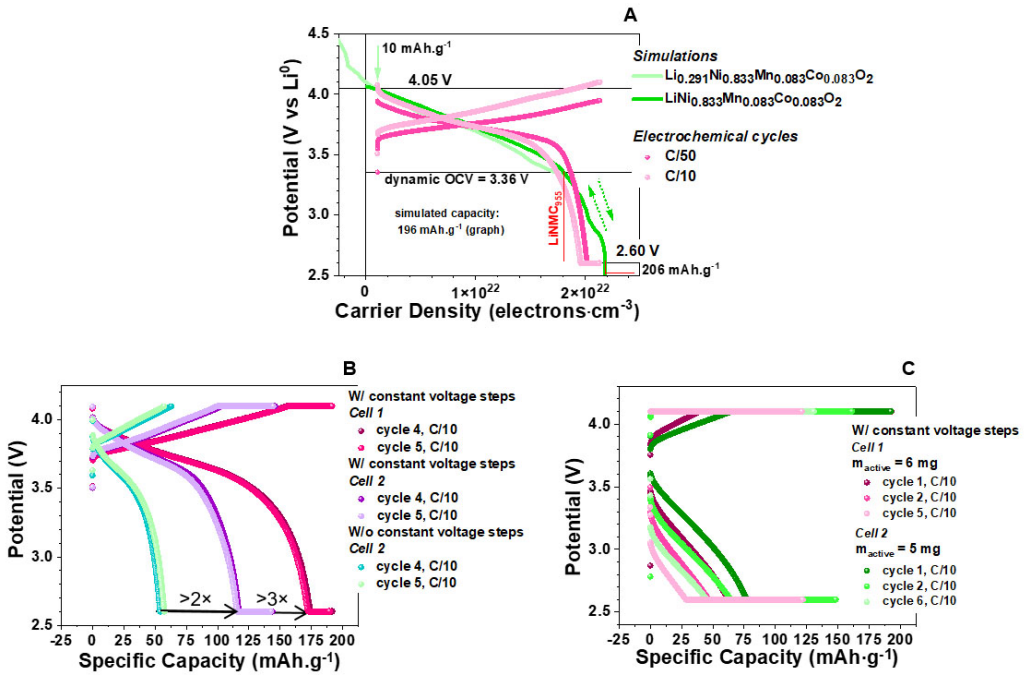

Figure 5. Electrochemical cycling of two cells, $Li^0/Li_6PS_5Cl/NMC_{955,}$ with a 57% NMC_{955}+38% Li_6PS_5Cl+3% C_{65}+2% SBR cathode simulated as ($LiNMC_{955}$) = $Li_{12}Ni_{10}MnCoO_{24}$ = $LiNi_{0.833}Mn_{0.083}Co_{0.083}O_2$ and ($Li_{0.29}NMC_{955}$) = $Li_7Ni_{20}Mn_2Co_2O_{48}$ = $Li_{0.291}Ni_{0.833}Mn_{0.083}Co_{0.083}O_2$. (A) Simulation of ($LiNMC_{955}$) and ($Li_{0.29}NMC_{955}$) versus experiments showing pinpoints for the electrochemical cycling, such as cut-offs and capacities; the discrepancies between simulated and experimental data are hypothesized to be due to the difference between simulated and experimental NMC_{955} stoichiometries, impedances and finite discharge rates; (B) two cells showing evidence for the necessity of including a constant voltage step that allows for ($Ni^{4+} \leftrightarrow Ni^{3+}$ and $Co^{4+} \leftrightarrow Co^{3+}$) completion. Cell 1 areal capacity is 0.167 $mAh.cm^{-2}$, and cell 2 0.434 $mAh.cm^{-2}$; the differences in capacities are mostly due to the lack of cycling at constant voltage; (C) Two cells with areal capacity of ~2 $mAh.cm^{-2}$ showing evidence for the necessity of including a constant voltage step. The areal capacity is also a determinant of the electrochemical performance and accounts for the differences in capacities and discharge voltages of cells in B and C. SBR: Styrene-butadiene rubber.

conditioning cycles with CV steps, followed by the same number of cycles without. Although preserving a coulombic efficiency of approximately 100%, the capacity is substantially different, as preconized. Even more substantial evidence is obtained for the cell cycling at a C-rate of C [Supplementary Figure 7B], where all the charge capacity is obtained at a CV. In contrast, the discharge capacity is partially obtained at a constant current, > 120 $mAh.g^{-1}$, and part at CV (< 70 $mAh.g^{-1}$) [Figure 4F]. Figure 5C shows the behavior of two cells containing 5 and 6 mg of active material, 10× the cells in Figure 5B. Both cell 1 and cell 2 achieve their highest capacity at C/10 after the first electrochemical cycle. After this, the cells experience a decrease in performance across subsequent cycles. In both cases, the capacity exhibits similar trends.

Pre/Post mortem TOF-SIMS analysis

TOF-SIMS is an advanced technique that provides detailed chemical and spatial information about the surfaces[53]. It works by bombarding the sample with a focused beam of high-energy ions, which release secondary ions that are analyzed to create a mass spectrum of the surface layers. By scanning the ion beam over the sample, spectra are obtained with the distribution of specific molecular species, or masses, from chosen areas of interest. In this study, TOF-SIMS was used to obtain molecular and spatial information about the degradation process of LPSCl/NMC_{955} composite cathodes[53]. Negative ion mass spectra of the cathode surface (acquired after sputter removal of the top surface, see Experimental section) displayed a multitude of peaks corresponding to secondary ions that can be associated with the different sample components, including $Ni_xO_y^-$ and $Co_xO_y^-$ ions representing the $LiNMC_{955}$ discharged cathode material, Cl^-,

S_x^- and PS_x^- ions representing the LPSCl electrolyte and C_xH^- ions representing the SBR binder.

Two cells were analyzed, a pristine and a cell that was cycled between 4.1 V and 2.6 V. The electrochemical profile of the cycled cell is shown in Supplementary Figure 3 and described in detail in Experimental Section. A comparison between the spectra from the uncycled pristine ("Fresh") and cycled cathode samples revealed a strong intensity increase of the SO_3^- and SO_4^- peaks upon cycling, particularly when compared with the (less oxidized) S_2O^- and S_3^- ions, respectively [Figure 6A]. In contrast, the PS^- and PO_2^- ions remained essentially unchanged upon cycling [Figure 6A]. These observations indicate that some of the most important chemical changes upon cycling are associated with oxidation of sulfur. Additionally, throughout the analysis, the oxidation of Mn^{3+} was not observed, even in the cycled samples. As indicated in Figure 2E, simulations indicate that manganese oxidation occurs above 4.1 V, where irreversible reactions occur. The absence of this oxidation in the analyzed samples highlights the importance of carefully defining charging limits and demonstrates how simulations are crucial in determining them.

The spatial distribution of the different components on the surface of the cycled cathode sample is visualized in the ion images [Figure 6B and C]. These images show a clear spatial separation between ions representing LPSCl and $LiNMC_{955}$, respectively, indicating that the particles of these components are well separated on the sample surface and that their respective localization is confidently visualized in the ion images. Furthermore, the sulfate ion image reveals a close correlation with the $LiNMC_{955}$ ion image, showing that the sulfates are mainly localized to the $LiNMC_{955}$ particles. This is a strong indication that the sulfur oxidation, found to be associated with cycling, mainly occurs by sulfur diffusion to the $LiNMC_{955}$ particles, rather than oxygen diffusion to the LPSCl particles. The latter assertion reinforces the necessity of not charging above 4.1 V to prevent the oxidation of $Li_{0.3}NMC_{955}$ avoiding reactions with sulfur, among other spurious reactions.

Pre/Post mortem Raman and calorimeter analysis

To evaluate the chemical and structural information of $LiNMC_{955}$ cathodes fabricated by wet processing, Raman measurements were conducted on as prepared and cycled $LiNMC_{955}$ electrodes [Figure 7A]. The Raman peak intensities were normalized on the highest peak intensity from LPSCl.

The main vibration modes for LPSCl show up as a prominent signal at 423 cm^{-1}, due to the symmetric stretching of (PS_4^{3-}), along with additional peaks at 197 cm^{-1} and 265 cm^{-1} and a band between ~500 cm^{-1} and 600 cm^{-1}, which come from asymmetric stretching of (PS_4^{3-}), as explained by Taklu *et al.*[54]. For $LiNMC_{955}$, most Raman-active vibrations are found in the 400-600 cm^{-1} range, with a strong signal approximately ~570 cm^{-1} from the A_{1g} mode of Ni, as reported by Li *et al.*[55]. There are also smaller signals between ~470 cm^{-1} and 610 cm^{-1}. A broader signal appears between ~1,200 cm^{-1} and 1,700 cm^{-1} where the presence of D and G bands arising from the carbon materials are observed[56-58], which could come from the carbon-coated aluminum foil supporting the cathode or from the conductive filler. This variety makes it difficult to pinpoint the exact source of these signals.

By analyzing Figure 7A, it becomes clear that most signals from the cathode's main components overlap in the 500-600 cm^{-1} range, making it challenging to assign these peaks specifically to the active material or the argyrodite phase, a common issue in the literature[56,59,60]. Even so, the main signal from the argyrodite phase remains clearly visible in both the as-prepared and cycled Raman spectra, confirming its presence in the cathode composite, already demonstrated with TOF-SIMS. Interestingly, the as-prepared cathode shows a stronger signal for the $LiNMC_{955}$ phase at ~570 cm^{-1} compared to the cycled version, which shows a lower overall intensity in the 500-600 cm^{-1} band. This difference may be due to degradation of the cathode

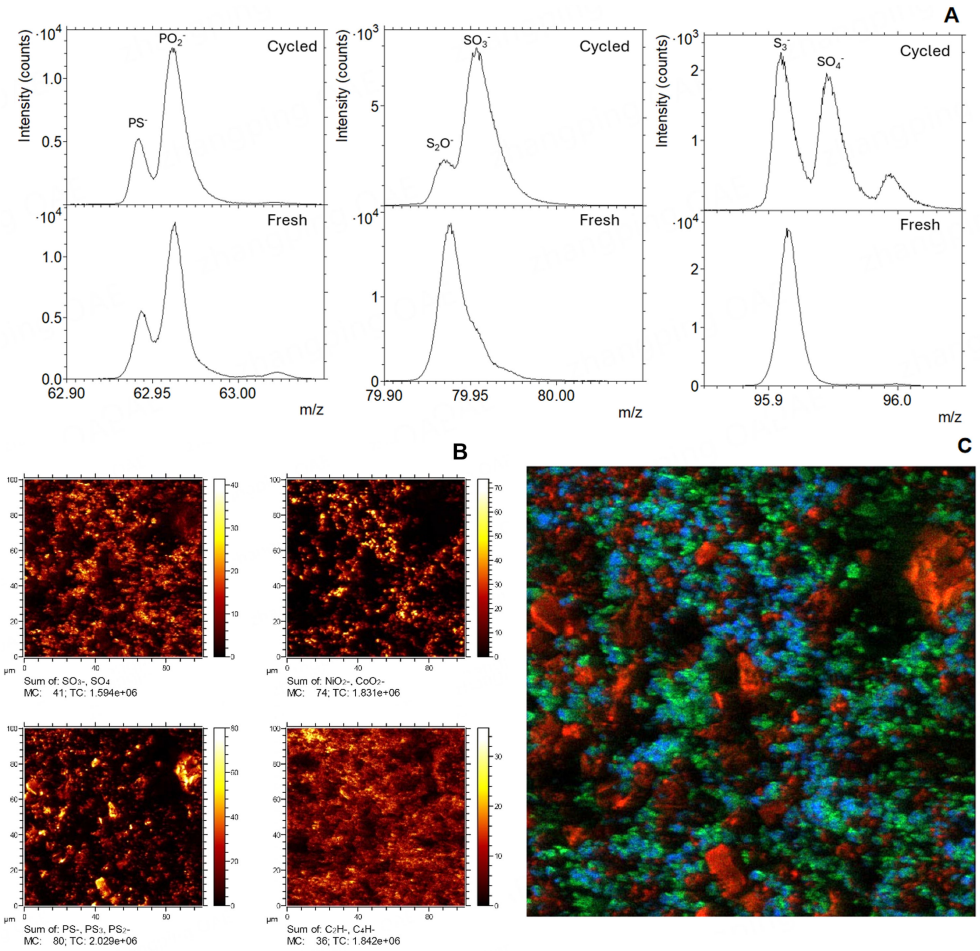

Figure 6. TOF-SIMS analysis of "Fresh" (pristine) and cycled electrode samples. (A) Negative ion spectra of pristine and cycled electrode samples focusing on peaks corresponding to PS^-/PO_2^- (left), S_2O^-/SO_3^- (center), and S_3^-/SO_4^- (right); (B) Ion images of secondary ions representing sulfates (top left), $LiNMC_{955}$ (top right), LPSCl (bottom left) and SBR binder (bottom right); (C) Three-colour overlay image (from B) showing LPSCl in red, sulfates in green and $LiNMC_{955}$ in blue. Field of view 100 × 100 μm^2. TOF-SIMS: Time-of-flight secondary ion mass spectrometry; LPSCl: Li_6PS_5Cl.

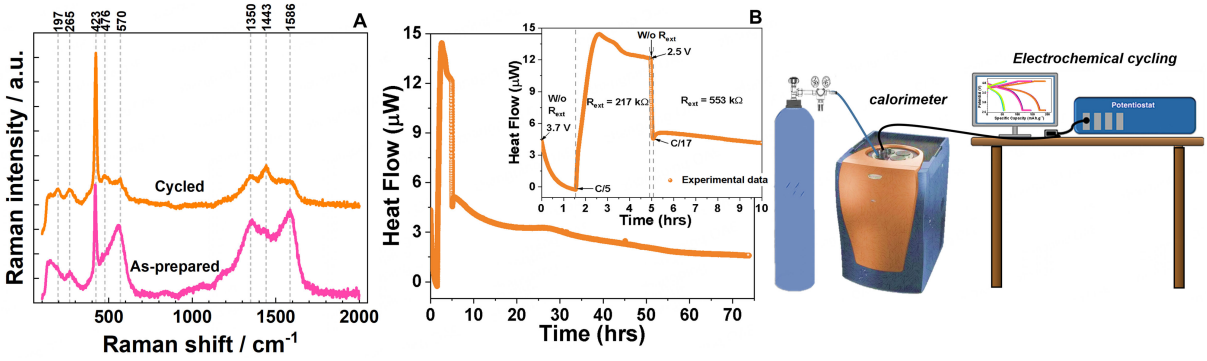

Figure 7. Analyses on pristine and post-mortem cycled cells. (A) Raman spectroscopy analysis as-prepared (pristine) and cycled cathode material; (B) Heat flow analysis on cell from Figure 4 at 30 °C considering different cycling states: (1) OCV (without external resistor), (2) R_{ext} = 217 kΩ, (3) OCV, and (4) R_{ext} = 553 kΩ. Schematics of the battery calorimeter set up on the right. OCV: Open circuit voltage.

material during cycling, reacting with the argyrodite LiPSCl, or to the potential damage while removing the cycled cathode from the pellet. In fact, the difference may be due to the formation of SO_3^- and SO_4^- on the surface of $LiNMC_{955}$, as shown by TOF-SIMS in Figure 6. The calorimeter analysis on the cell from Figure 4 obtained while discharging from 3.7 V shows that the higher the discharge current the greater the amount of heat released [Figure 7B]. This may indicate that oxygen is mostly released immediately after the beginning of discharge at higher C-rates (exothermic reaction), as shown in the inset of Figure 4B. More than 2.2 h are necessary to start stabilizing the heat flow at ~C/5, with the first hour corresponding to a pronounced exothermic variation of 14.6 μW.

CONCLUSIONS

This study demonstrates the effectiveness of the NMC_{955} cathode, prepared using a novel simulation-supported wet preparation method, in a Li^0/LPSCl/NMC_{955} all-solid-state cell. The cell operates efficiently at room temperature without additional interlayers or applied pressure. A cost-effective and environmentally friendly binder, SBR, was employed as an alternative to traditional PVDF, enhancing processability while maintaining performance, thereby providing a viable preparation method for all-solid-state lithium batteries.

The proposed cathode enables stable and long-lasting cell performance, achieving theoretical capacities across various C-rates (C/50 → 3C) and sustaining a high-rate capability for C. This was made possible through the inclusion of a CV step during both charge and discharge, which showcased a near 100% coulombic efficiency over 200 cycles. The first 70 cycles spanned a wide range of C-rates, while the remaining 130 cycles were conducted at C C-rate, all at 25 °C without applied pressure. This methodology emphasizes the importance of conditioning and battery management systems grounded in theoretical studies to advance efficiency and high-rate performance.

Theoretical insights, supported by simulations of chemical potential versus charge carrier density and DOS for $LiNMC_{955}$ and $Li_{0.3}NMC_{955}$, demonstrated that tailored cycling protocols significantly extend cycle life. The approach minimizes oxygen release and its reaction with LPSCl, reduces overcharge-induced sulfur and sulfate formation, and avoids the formation of detrimental Mn^{3+} and Ni^{2+} during over-discharge. This ensures the structural integrity of the cathode and eliminates the adverse effects of the $Mn^{3+/4+}$ redox pair, while leveraging the stabilizing influence of the $Co^{3+/4+}$ redox couple.

Advanced analytical techniques, including sheet resistance/Hall effect, atomic force microscopy/SKPM, TOF-SIMS, Raman spectroscopy, and battery calorimetry, complemented the electrochemical and SEM/EDX analyses, providing robust validation of the findings. These methods clarified the pivotal role of the cathode in shaping the electrochemical cycle and determining the cycle life of the Li^0/LPSCl/NMC_{955} all-solid-state battery.

The results position NMC_{955} as a sustainable and high-performance cathode material for next-generation solid-state batteries, offering a pathway to high-power and high-energy-density solutions while deviating from environmentally unsustainable components. This study highlights the value of "following the electrons" to derive quantitative and qualitative insights, enabling optimized cycling protocols and advancing the design of solid-state battery systems.

DECLARATIONS

Authors' contributions

Conceptualization: Gomes, B. M.; Baptista, M. C.; Orue, A.; Braga, M. H.

Data collection: Gomes, B. M.; Baptista, M. C.; Terlicka, S.; Orue, A.; Dhrubajyoti, B.; Sjövall, P.; Zamperlin, N.; Braga, M. H.
Data analysis: Gomes, B. M.; Baptista, M. C.; Orue, A.; Dhrubajyoti, B.; Braga, M. H.
Simulations: Braga, M. H.
Writing-original draft: Gomes, B. M.; Baptista, M. C.; Terlicka, S.; Orue, A.; Dhrubajyoti, B.; Braga, M. H.
Funding acquisition: Orue, A.; Smajic, J.; Kekkonen, V.; Vonk, W.; Tron, A.; Braga, M. H.; Ahniyaz, A.
Supervision: Braga, M. H.
State-of-the-art insights, writing-review, editing, and approval of final version: Gomes, B. M.; Baptista, M. C.; Orue, A.; Dhrubajyoti, B.; Terlicka, S.; Sjövall, P.; Zamperlin, N.; Fonseca, C.; Smajic, J.; Kekkonen, V.; Vonk, W.; Tron, A.; Schena, A.; Ahniyaz, A.; Braga, M. H.

Availability of data and materials
All datasets generated for this study are included in the article/Supplementary Materials.

Financial support and sponsorship
This project has received funding from the European Union's Horizon Europe research and innovation programme under grant agreement No. 101069686 (PULSELiON). Views and opinions expressed are those of the authors only and do not necessarily reflect those of the European Union or CINEA. Neither the European Union nor the granting authority can be held responsible.

Conflicts of interest
All authors declared that there are no conflicts of interest.

Ethical approval and consent to participate
Not applicable.

Consent for publication
Not applicable.

REFERENCES
1. Randau, S.; Weber, D. A.; Kötz, O.; et al. Benchmarking the performance of all-solid-state lithium batteries. *Nat. Energy.* **2020**, *5*, 259-70. DOI
2. Hou, D.; Xu, Z.; Yang, Z.; et al. Effect of the grain arrangements on the thermal stability of polycrystalline nickel-rich lithium-based battery cathodes. *Nat. Commun.* **2022**, *13*, 3437. DOI PubMed PMC
3. Chen, S.; Wen, K.; Fan, J.; Bando, Y.; Golberg, D. Progress and future prospects of high-voltage and high-safety electrolytes in advanced lithium batteries: from liquid to solid electrolytes. *J. Mater. Chem. A.* **2018**, *6*, 11631-63. DOI
4. Vinayak, A. K.; Li, M.; Huang, X.; et al. Circular economies for lithium-ion batteries and challenges to their implementation. *Next. Mater.* **2024**, *5*, 100231. DOI
5. Man, Q.; An, Y.; Shen, H.; et al. MXenes and their derivatives for advanced solid-state energy storage devices. *Adv. Funct. Mater.* **2023**, *33*, 2303668. DOI
6. Tron, A.; Hamid, R.; Zhang, N.; Beutl, A. Rational optimization of cathode composites for sulfide-based all-solid-state batteries. *Nanomaterials* **2023**, *13*, 327. DOI PubMed PMC
7. Liu, W.; Li, D.; Liu, Y.; Luo, D.; Xu, R. A critical review of single-crystal $LiNi_xMn_yCo_{1-x-y}O_2$ cathode materials. *Renewables* **2024**, *2*, 25-51. DOI
8. Bin, A. S. A. D. A.; Imaduddin, I. S.; Majid, S.; et al. Nickel-rich nickel-cobalt-manganese and nickel-cobalt-aluminum cathodes in lithium-ion batteries: Pathways for performance optimization. *J. Cleaner. Prod.* **2024**, *435*, 140324. DOI
9. Saaid, F. I.; Kasim, M. F.; Winie, T.; et al. Ni-rich lithium nickel manganese cobalt oxide cathode materials: a review on the synthesis methods and their electrochemical performances. *Heliyon* **2024**, *10*, e23968. DOI PubMed PMC
10. Das, D.; Manna, S.; Puravankara, S. Electrolytes, additives and binders for NMC cathodes in Li-ion batteries-a review. *Batteries* **2023**,

9, 193. DOI

11. Wang, Q.; Wang, Z.; Li, X.; Zhu, Y.; Gao, P. Synthesis and characterization of Co-free NMA cathodes for fast charging lithium-ion batteries. *J. Alloys. Compd.* **2023**, *955*, 170226. DOI
12. Li, W.; Lee, S.; Manthiram, A. High-Nickel NMA: a cobalt-free alternative to NMC and NCA cathodes for lithium-ion batteries. *Adv. Mater.* **2020**, *32*, 2002718. DOI
13. Maia, B. A.; Gomes, B. M.; Guerreiro, A. N.; Santos, R. M.; Braga, M. H. Cathodes pinpoints for the next generation of energy storage devices: the $LiFePO_4$ case study. *J. Phys. Mater.* **2024**, *7*, 025001. DOI
14. Baptista, M. C.; Gomes, B. M.; Capela, D.; et al. Conditioning solid-state anode-less cells for the next generation of batteries. *Batteries* **2023**, *9*, 402. DOI
15. Braga, M. H.; Stockhausen, V.; Oliveira, J. C.; Ferreira, J. A. The role of defects in Li_3ClO solid electrolyte: calculations and experiments. *MRS. Online. Proceedings. Library.* **2013**, *1526*, 905. DOI
16. Baptista, M. C.; Gomes, B. M.; Vale, A. B.; Braga, M. H. In-series all-solid-state anode-less cells. *J. Energy. Storage.* **2024**, *102*, 113983. DOI
17. Li, S.; Meng, X.; Yi, Q.; et al. Structural and electrochemical properties of $LiMn_{0.6}Fe_{0.4}PO_4$ as a cathode material for flexible lithium-ion batteries and self-charging power pack. *Nano. Energy.* **2018**, *52*, 510-6. DOI
18. Gu, H.; Li, W.; Li, Q.; et al. Electrochemical properties of $Li_4Ti_5O_{12}$ coated $LiMn_{0.6}Fe_{0.4}PO_4$ prepared by rheological phase reaction method. *J. Electrochem. Soc.* **2024**, *171*, 040502. DOI
19. Nguyen, M. T.; Pham, H. Q.; Berrocal, J. A.; Gunkel, I.; Steiner, U. An electrolyte additive for the improved high voltage performance of $LiNi_{0.5}Mn_{1.5}O_4$ (LNMO) cathodes in Li-ion batteries. *J. Mater. Chem. A.* **2023**, *11*, 7670-8. DOI
20. Jiang, H.; Zeng, C.; Zhu, W.; et al. Boosting cycling stability by regulating surface oxygen vacancies of LNMO by rapid calcination. *Nano. Res.* **2024**, *17*, 2671-7. DOI
21. Hofmann, A.; Höweling, A.; Bohn, N.; Müller, M.; Binder, J. R.; Hanemann, T. Additives for cycle life improvement of high-voltage LNMO-based Li-ion cells. *ChemElectroChem* **2019**, *6*, 5255-63. DOI
22. Malik, M.; Chan, K. H.; Azimi, G. Review on the synthesis of $LiNi_xMn_yCo_{1-x-y}O_2$ (NMC) cathodes for lithium-ion batteries. *Mater. Today. Energy.* **2022**, *28*, 101066. DOI
23. Li, M.; Lu, J. Cobalt in lithium-ion batteries. *Science* **2020**, *367*, 979-80. DOI
24. Noerochim, L.; Suwarno, S.; Idris, N. H.; Dipojono, H. K. Recent development of nickel-rich and cobalt-free cathode materials for lithium-ion batteries. *Batteries* **2021**, *7*, 84. DOI
25. Xu, C.; Märker, K.; Lee, J.; et al. Bulk fatigue induced by surface reconstruction in layered Ni-rich cathodes for Li-ion batteries. *Nat. Mater.* **2021**, *20*, 84-92. DOI
26. Kim, U.; Kuo, L.; Kaghazchi, P.; Yoon, C. S.; Sun, Y. Quaternary layered Ni-rich NCMA cathode for lithium-ion batteries. *ACS. Energy. Lett.* **2019**, *4*, 576-82. DOI
27. Emley, B.; Wu, C.; Zhao, L.; et al. Impact of fabrication methods on binder distribution and charge transport in composite cathodes of all-solid-state batteries. *Mater. Futures.* **2023**, *2*, 045102. DOI
28. Gomes, B. M.; Ribeiro, M. J. F.; Braga, M. H. A perspective on the building blocks of a solid-state battery: from solid electrolytes to quantum power harvesting and storage. *J. Mater. Chem. A.* **2024**, *12*, 690-722. DOI
29. Yu, C.; Ganapathy, S.; Hageman, J.; et al. Facile synthesis toward the optimal structure-conductivity characteristics of the argyrodite Li_6PS_5Cl solid-state electrolyte. *ACS. Appl. Mater. Interfaces.* **2018**, *10*, 33296-306. DOI
30. Nikodimos, Y.; Huang, C.; Taklu, B. W.; Su, W.; Hwang, B. J. Chemical stability of sulfide solid-state electrolytes: stability toward humid air and compatibility with solvents and binders. *Energy. Environ. Sci.* **2022**, *15*, 991-1033. DOI
31. Wang, Z.; Xia, J.; Ji, X.; et al. Lithium anode interlayer design for all-solid-state lithium-metal batteries. *Nat. Energy.* **2024**, *9*, 251-62. DOI
32. Liu, Y.; Wang, C.; Yoon, S. G.; et al. Aluminum foil negative electrodes with multiphase microstructure for all-solid-state Li-ion batteries. *Nat. Commun.* **2023**, *14*, 3975. DOI PubMed PMC
33. Zhong, X.; Han, J.; Chen, L.; et al. Binding mechanisms of PVDF in lithium ion batteries. *Appl. Surf. Sci.* **2021**, *553*, 149564. DOI
34. Cordner, A.; Brown, P.; Cousins, I. T.; et al. PFAS Contamination in europe: generating knowledge and mapping known and likely contamination with "expert-reviewed" journalism. *Environ. Sci. Technol.* **2024**, *58*, 6616-27. DOI
35. Sonne, C.; Jenssen, B. M.; Rinklebe, J.; et al. EU need to protect its environment from toxic per- and polyfluoroalkyl substances. *Sci. Total. Environ.* **2023**, *876*, 162770. DOI
36. Singer, C.; Schmalzbauer, S.; Daub, R. Influence of the slurry composition on thin-film components for the wet coating process of sulfide-based all-solid-state batteries. *J. Energy. Storage.* **2023**, *68*, 107703. DOI
37. Gao, J.; Hao, J.; Gao, Y.; et al. Scalable wet-slurry fabrication of sheet-type electrodes for sulfide all-solid-state batteries and performance enhancement via optimization of Ni-rich cathode coating layer. *eTransportation* **2023**, *17*, 100252. DOI
38. Ruhl, J.; Riegger, L. M.; Ghidiu, M.; Zeier, W. G. Impact of solvent treatment of the superionic argyrodite Li_6PS_5Cl on solid-state battery performance. *Adv. Energy. Sustain. Res.* **2021**, *2*, 2000077. DOI
39. Tan, D. H. S.; Banerjee, A.; Deng, Z.; et al. Enabling thin and flexible solid-state composite electrolytes by the scalable solution process. *ACS. Appl. Energy. Mater.* **2019**, *2*, 6542-50. DOI
40. Rolandi, A. C.; de, M. I.; Casado, N.; Forsyth, M.; Mecerreyes, D.; Pozo-gonzalo, C. Unlocking sustainable power: advances in aqueous processing and water-soluble binders for NMC cathodes in high-voltage Li-ion batteries. *RSC. Sustain.* **2024**, *2*, 2125-49. DOI

41. Demiryürek, R.; Gürbüz, N.; Hatipoglu, G.; et al. Roll-to-roll manufacturing method of aqueous-processed thick $LiNi_{0.5}Mn_{0.3}Co_{0.2}O_2$ electrodes for lithium-ion batteries. *Int. J. Energy. Res.* **2021**, *45*, 21182-94. DOI
42. Surace, Y.; Jahn, M.; Cupid, D. M. The rate capability performance of high-areal-capacity water-based NMC811 electrodes: the role of binders and current collectors. *Batteries* **2024**, *10*, 100. DOI
43. Isozumi, H.; Kubota, K.; Tatara, R.; et al. Impact of newly developed styrene-butadiene-rubber binder on the electrode performance of high-voltage $LiNi_{0.5}Mn_{1.5}O_4$ electrode. *ACS. Appl. Energy. Mater.* **2020**, *3*, 7978-87. DOI
44. Yabuuchi, N.; Kinoshita, Y.; Misaki, K.; Matsuyama, T.; Komaba, S. Electrochemical properties of $LiCoO_2$ electrodes with latex binders on high-voltage exposure. *J. Electrochem. Soc.* **2015**, *162*, A538. DOI
45. Wu, Q.; Ha, S.; Prakash, J.; Dees, D. W.; Lu, W. Investigations on high energy lithium-ion batteries with aqueous binder. *Electrochim. Acta.* **2013**, *114*, 1-6. DOI
46. Kasnatscheew, J.; Börner, M.; Streipert, B.; et al. Lithium ion battery cells under abusive discharge conditions: electrode potential development and interactions between positive and negative electrode. *J. Power. Sources.* **2017**, *362*, 278-82. DOI
47. Dose, W. M.; Xu, C.; Grey, C. P.; De, V. M. F. Effect of anode slippage on cathode cutoff potential and degradation mechanisms in Ni-rich Li-ion batteries. *Cell. Rep. Phys. Sci.* **2020**, *1*, 100253. DOI
48. Zhang, S. S. The effect of the charging protocol on the cycle life of a Li-ion battery. *J. Power. Sources.* **2006**, *161*, 1385-91. DOI
49. Kresse, G.; Hafner, J. Ab initio molecular dynamics for liquid metals. *Phys. Rev. B.* **1993**, *47*, 558. DOI
50. Perdew, J. P.; Wang, Y. Accurate and simple analytic representation of the electron-gas correlation energy. *Phys. Rev. B.* **1992**, *45*, 13244-9. DOI
51. Trasatti, S. The absolute electrode potential: an explanatory note (Recommendations 1986). *Pure. Appl. Chem.* **1986**, *58*, 955-66. DOI
52. Nipan, G. D. Isobaric-isothermal polyhedra of solid solutions in the Li-Ni-Mn-Co-O system. *Inorg. Mater.* **2021**, *57*, 518-23. DOI
53. Walther, F.; Koerver, R.; Fuchs, T.; et al. Visualization of the interfacial decomposition of composite cathodes in argyrodite-based all-solid-state batteries using time-of-flight secondary-ion mass spectrometry. *Chem. Mater.* **2019**, *31*, 3745-55. DOI
54. Taklu, B. W.; Su, W.; Nikodimos, Y.; et al. Dual CuCl doped argyrodite superconductor to boost the interfacial compatibility and air stability for all solid-state lithium metal batteries. *Nano. Energy.* **2021**, *90*, 106542. DOI
55. Li, X.; Chang, K.; Abbas, S. M.; et al. Silver nanocoating of $LiNi_{0.8}Co_{0.1}Mn_{0.1}O_2$ cathode material for lithium-ion batteries. *Micromachines* **2023**, *14*, 907. DOI
56. Byeon, Y.; Yang, S.; Yang, G.; et al. Conductive carbon embedded beneath cathode active material for longevity of solid-state batteries. *J. Mater. Chem. A.* **2024**, *12*, 8359-69. DOI
57. Jung, Y. H.; Lim, C. H.; Kim, D. K. Graphene-supported $Na_3V_2(PO_4)_3$ as a high rate cathode material for sodium-ion batteries. *J. Mater. Chem. A.* **2013**, *1*, 11350-4. DOI
58. Araño, K. G.; Yang, G.; Armstrong, B. L.; et al. Carbon coating influence on the formation of percolating electrode networks for silicon anodes. *ACS. Appl. Energy. Mater.* **2023**, *6*, 11308-21. DOI
59. Nam, J. S.; To, A. R. W.; Lee, S. H.; et al. Densification and charge transport characterization of composite cathodes with single-crystalline $LiNi_{0.8}Co_{0.15}Al_{0.05}O_2$ for solid-state batteries. *Energy. Storage. Mater.* **2022**, *46*, 155-64. DOI
60. Rajagopal, R.; Subramanian, Y.; Jung, Y. J.; Kang, S.; Ryu, K. Rapid Synthesis of highly conductive Li_6PS_5Cl argyrodite-type solid electrolytes using pyridine solvent. *ACS. Appl. Energy. Mater.* **2022**, *5*, 9266-72. DOI